Competition between ordered morphologies of functionalized silver nanoparticles elucidated by a joint experimental and multiscale theoretical study

David Loffreda, Nathalie Tarrat, Corinne Lacaze-Dufaure, Franck Rabilloud, Katia Fajerwerg, Myrtil Kahn, Vincent Collière, Christine Lepetit, Pierre Fau

Nano Today 62 (2025) 102662

Contents lists available at ScienceDirect

Nano Today

journal homepage: www.elsevier.com/locate/nanotoday

Competition between ordered morphologies of functionalized silver nanoparticles elucidated by a joint experimental and multiscale theoretical study

David Loffreda [a,*,1], Nathalie Tarrat [b,*,2], Corinne Lacaze-Dufaure [c,3], Franck Rabilloud [d,4], Katia Fajerwerg [e,5], Myrtil L. Kahn [e,6], Vincent Collière [e,7], Christine Lepetit [e,8], Pierre Fau [f,*,9]

[a] CNRS, ENS de Lyon, Université Claude Bernard Lyon 1, LCH, UMR 5182, 69342 Lyon Cedex 07, France
[b] CEMES, Université de Toulouse, CNRS, 31055 Toulouse, France
[c] CIRIMAT, Toulouse INP, Université de Toulouse, CNRS, 4 Allée Emile Monso - BP 44362, 31030 Toulouse Cedex 4 - France
[d] Université Claude Bernard Lyon 1, CNRS, Institut Lumière Matière, UMR 5306, F69100 Villeurbanne, France
[e] LCC-CNRS, Université de Toulouse, CNRS, UPS, 31077 Toulouse Cedex 04, France
[f] Laboratoire de Physique et Chimie des Nano-Objets, INSA Toulouse, CNRS, UMR 5215, Université Toulouse 3, F-31077 Toulouse Cedex 4, France

ARTICLE INFO

Keywords:
Functionalized silver nanoparticles
Support and solvent environmental effects
High resolution transmission electron microscopy
Density functional theory
Multiscale modeling

ABSTRACT

A multiscale approach, combining density functional theory models of functionalized silver nanoparticles and extended surfaces, is introduced to predict the competition between ordered nanoparticles at experimentally relevant size. An original theoretical descriptor, named synthesis energy, is defined and validated by high resolution transmission electron microscopy characterizations of silver nanoparticles synthesized in a solvated amine and amidine medium. Microscopy images show that icosahedral clusters cover 90 % of statistics around 7 nm, with very minority face-centered cubic particles (1 %). This trend is counter-intuitive compared to face-centered cubic morphologies reported in the literature. The *ab initio* models show a larger stability for octylamine over methyl amidine ligands on small silver nanoparticles (1.5 nm). At larger size (2.5 nm), the octylamine-covered silver nanocluster models indicate a clear preference for icosahedra. To reach the experimental size, the computed synthesis energy is decomposed into several contributions and shows the prevalence of the clean nanoparticle cohesion energy normalized by its surface area, over the ligand adsorption strength, the precursor dissociation and the adhesion of the cluster on the support. A mathematical model fitting *ab initio* data and predicting this cohesion energy at any size, relevantly captures the competition between morphologies, by showing a net preference for icosahedra at 7 nm, in agreement with experiments.

Introduction

The theoretical prediction of metallic nanoparticle morphology from a particular synthesis process is a tremendous challenge. The major difficulty is the development of a sufficiently accurate methodology able to predict the relative stability of different morphologies from small clusters of a few nanometers to very large particles of several hundreds of nanometers. An interesting way to examine such a question is the

* Corresponding authors.
E-mail addresses: david.loffreda@ens-lyon.fr (D. Loffreda), nathalie.tarrat@cemes.fr (N. Tarrat), pfau@insa-toulouse.fr (P. Fau).
[1] 0000–0001-9912–7965
[2] 0000–0002-0909–0001
[3] 0000–0003-3151–2685
[4] 0000–0002-5011–3949
[5] 0000–0002-3897–3380
[6] 0000–0003-3079–5759
[7] 0000–0003-1937–6991
[8] 0000–0002-0008–9506
[9] 0000–0003-0014–2511

https://doi.org/10.1016/j.nantod.2025.102662
Received 12 September 2024; Received in revised form 12 December 2024; Accepted 5 February 2025
Available online 20 February 2025

development of two extreme models, one for clusters representing small nanoparticles and the other one for extended periodic surfaces modeling wide facets of very large particles. Although there exists one *ab initio* method, Density Functional Theory (DFT), allowing high level calculations of these extreme models, to date no first-principles methodology is accurate enough to cross sizes and predict nanoparticle properties at experimentally relevant intermediate sizes. In this context, further theoretical models are to be developed in order to investigate all the sizes, for which accurate methods could not be considered. Moreover, no theoretical descriptor is currently available in the literature for investigating the morphological competition in the context of chemically-synthesized metallic nanoparticles.

Functionalized silver nanoparticles (Ag NPs) are a probative example in the literature showing numerous synthesis processes [1–5] providing a vast range of sizes and morphologies of potential interest in various applications covering catalysis, [6,7] optics, [7,8] drug delivery, [9] theranostics [10] and antimicrobials [11–13]. Three high symmetries (face-centered cubic *FCC* or *Oh*, icosahedral *Ih* and decahedral *D*5*h*) are found in equivalent statistics for commercial Ag NPs in the range 1–10 nm kept in a carbon matrix. [11] Among the synthesis protocols from academic research (see an overview of the literature in Table S25 of the Supporting Information, Section 10), Ag NPs can be formed by either various physical routes, starting from Ag bulk [14–20] to Ag_2O powders [21], or chemical routes, most of them using $AgNO_3$ precursors [8, 22–45].

In the case of the physical route, the choice of the support and the heat treatment have an impact on size distribution and on competition between morphologies. On amorphous silica with a treatment at 600°C avoiding any kinetic trapping, a majority of icosahedral nanoparticles (60 %) has been detected from high-resolution transmission electron microscopy (HRTEM) up to 7 nm, whereas decahedral shape becomes predominant (90 %) in the range 7–11 nm, and *FCC* single crystals dominate morphology statistics above 11 nm (90 %). [16] These interesting results are different from those reported on another study, where Ag NPs are grown on silicon, at a higher temperature (800–1000°C). [21] A preference for icosahedral and decahedral nanoparticles is found in this case up to 100 nm. In addition, Ag NPs synthesized in vacuum, in the range 309–923 atoms, [18,19] and supported on amorphous carbon show a prevalence of *FCC* clusters. The icosahedral symmetry becomes preferential (below 3000 atoms), when Ag NPs are exposed to air. [20] Hence none of the morphology statistics obtained by physical synthesis routes reconcile with commercial Ag NP products.

Regarding the chemical route, the sizes and morphologies of functionalized Ag NPs also depend on the synthesis protocol, including e.g. the choice of the silver precursors, reducing and capping agents, temperature, solvent and kinetic trapping. *FCC* nanoparticles have been frequently synthesized in the range 1–100 nm. [23,26,29,30,35,36,44, 45] The choice of the silver precursor $AgNO_3$ [35,44], Ag_2NO_3 [45], Ag-acetate [26] and the capping agent hexadecylamine [26,29,35] offer a large variety of sizes in the range 1–24 nm by keeping the *FCC* symmetry. Other synthesis protocols have also yielded nanocubes and *FCC* nanoparticles, in the range 20–100 nm, by also considering $AgNO_3$ as precursor with alternate capping agents (polyvinylpyrrolidone, [23,30] ethylene glycol, [36] and citrate [30]). By using $AgNO_3$ precursors and amidinate ligands (such as bis(2-pyridyl)-formamidinate), very small functionalized Ag clusters (Ag52, Ag53) could be stabilized in a *FCC* structure, [45] in contrast with a previous study at an even smaller size (Ag21, Ag22) with dipyridylamido protecting ligands, which had shown icosahedral nanoparticle cores. [42]

Surprinsingly, the *Ih* forms have often been detected from HRTEM measurements [31,32,34,37,39,41] and found majority, in synthesis conditions similar to those yielding *FCC* clusters ($AgNO_3$ precursor and capping agents, such as polyvinylpyrrolidone [33,34,37,41], citrate, [37] tartrates, [39] diols, [31] oleylamine, [32] or ammonia [34]) and equivalent large range of sizes (2–150 nm). Other authors have addressed a preference for decahedral shapes in the range 35–120 nm, [28] or at small sizes with thiolates, [40,43] whereas in similar synthesis conditions, another study indicates no preference between *Ih* and *D*5*h* nanoparticles up to 100 nm. [33]

In addition, over the last twenty years, amidinate [38] or mesityl [24] precursors have been associated several times with amine ligands (such as diamine, [22] tertiary alkyl amine, [25] hexadecylamine, [24, 38] oleylamine [27]) for the synthesis of Ag NPs, without focusing the discussion on the structural properties. In summary, in this vast bibliography related to functionalized Ag NPs with different synthesis protocols, a rationale is missing since reliable predictions of favored morphologies depending on the synthesis environment can not be sketched out from the literature. Therefore there is a need for theoretical modeling aiming to evaluate all the competing effects and contributions leading to a preferred symmetry. [46,47]

Over the last two decades, intensive theoretical efforts have been conceded to explore the relative stability of Ag nanoclusters and its competitive high symmetries, as a function of size and morphological complexity, first in vacuum with various effective atomic or semi-empirical potentials [48–59] (up to 10,000 atoms or 8 nm), or with *ab initio* methods [19,58,60,61] at smaller size (below 3 nm). The different theoretical conclusions exposed in all these studies regarding the competitive morphologies (*FCC* versus icosahedral or decahedral symmetries) reflect a clear lack of highly controlled measurements in vacuum helping to validate all these approaches. Such discussion has been opened recently on the basis of new experimental results aiming to advance on this question. [18,19] Beyond idealistic models in vacuum, other DFT studies have reported on the interaction of various amine-based molecules or thiols either on Ag NPs [62–66] or on Ag extended surfaces [67–71], at a restricted size (below 3 nm) due to the computational cost. Although these DFT models are not representative of much larger Ag NPs, they can be useful to parametrize force fields or effective potentials, in order to describe complex systems such as Ag NPs supported on silica. [72,73] In addition, *ab initio* molecular dynamics at the DFT level is also useful to accurately explore the impact of several combined environment effects on the morphological evolution of Ag NPs exposed to air, according to the fair agreement with directly comparable experiments. [20,66] To reach large size functionalized Ag NPs and tackle the difficult question of global optimization, more approximate theoretical methods ranging from tight-binding density functional theory (DFTB) to force fields [74] can be implemented in a multiscale modeling [75–77] assisted by several mathematical techniques such as classical molecular dynamics, [77,78] genetic algorithm, Monte Carlo simulations [76] and machine learning. [79] Although powerful to explore complex configurational space, these approaches show limits when the synthesis environment and interfacial physico-chemical processes have to be considered explicitly and accurately. In summary, both multiscale modeling predicting the morphological competition of chemically-synthesized Ag NPs and rationalizing environment effects, and achievable DFT models of large functionalized Ag NPs are missing in the literature to date.

In this work, we tackle the challenge of proposing a multiscale approach aiming to determine the relative stability of high symmetries in competition with a sufficient accuracy, in the experimentally relevant size (3–10 nm) out of reach for *ab initio* methods. We introduce a global chemical equation describing the synthesis of metallic nanoparticles from two different organometallic precursors, and a corresponding original descriptor, named synthesis energy, which captures the reaction energy. This approach is applied for Ag NPs synthesized and stabilized in solution with amine and amidine ligands. In addition, the synthesis energy is decomposed into several contributions related to the key steps involved in the synthesis. Those components are compared in various chemical environments (ligands, solvent, support). A mathematical function predicting at any size the main contribution, called clean nanoparticle cohesion energy normalized by its surface area, is then developed by considering general properties of ordered nanoparticles. To compute the synthesis energy, determine the relative weights of its

contributions and fit the mathematical function, DFT calculations are performed for functionalized Ag NPs (in the range 1–3.5 nm) and extended surfaces representing large facets. The predictions of the multiscale approach are validated by comparison with experimental characterization of chemically-synthesized Ag NPs of diameter around 7 nm.

Results and discussion

Experiments

In colloidal chemistry, the choice of the metal precursor, which is not innocent toward the resulting properties of the synthesized NPs, is a key parameter for a well-controlled synthesis of Ag NPs. [80] To date, there exist only very few examples of metallorganic Ag precursors. [81] In this work, solid silver amidinate precursors are prepared by following a procedure inspired by Lim et al.'s works [82] (see Materials and Methods and the Supporting Information, Section 1). In a previous study the affinity of the amidine (**AMD**) moiety for Ag NPs surface has been experimentally evidenced by Surface Enhanced Raman Spectroscopy (SERS) and theoretical modeling. [38] By using methyl (precursor **1**) [38] or butyl (precursor **2**) [83] amidinate silver precursors (Fig. 1a, the alkyl group being changed on the central carbon), well-defined Ag NPs could be synthesized under very mild reaction conditions (40°C), with mean size distributions of 6.2 ± 1.4 nm for **1** and 6.9 ± 1.5 nm for **2** (Fig. 1b, see the histogram of NP size distribution for precursor **1**). The use of methyl and butyl amidinate precursors in our study has been dictated by the choice of an organometallic precursor that do not contain any halide. In that way, we ensure that the Ag NPs will be chemically pure and only stabilized by amine ligands that are present in the reaction medium. The two precursors present different thermal stability evaluated by Thermal Gravimetric Analysis (TGA) (see Fig. S1 in the Supporting Information, Section 1) and the amidine ligands released in the medium after hydrogenolysis participate to the NPs stabilization, as well as the added hexadecylamine **HDA** ligand. The complementary role of these ligands allow the effective stabilization of Ag NPs in colloidal solution. As expected, the mean size of the Ag NPs is slightly modified by the chain length of the substituent in the **AMD** precursor (Fig. 1b for **1** and Fig. S2 for **2**, Supporting Information, Section 1). Thanks to the conjoint stabilizing effects of **HDA/AMD** ligands, our synthesized Ag NPs at 6–7 nm are stable enough for allowing an ex-situ morphological characterization. We have performed HRTEM for the determination of the different morphologies exhibited by the Ag NPs deposited on amorphous carbon. Small size NPs crystallize under different possible morphologies, either polycrystalline (multiple-twinned structures such as regular decahedron or defective Marks-decahedron *D*5*h* or icosahedron *Ih*) or monocrystalline *FCC* (*Oh*) structures (Fig. 1a). All along these measurements, we have not observed any morphological transition during the exposure of Ag NPs to the microscope electron beam, meaning that our nanoparticles are maintained in equilibrium on amorphous carbon support. Our methodology for recognizing the different morphologies of Ag NPs relies on the significant work of Koga et al. [84], who experimentally identified by HRTEM the *Ih*, *D*5*h*, and *FCC* geometries of Au NPs, from various tilting angles of the sample holder, with multislice simulations of these structures. Thanks to their work on identifying the structural features of these different NPs, we were able to recognize, among our own HRTEM images (30 high resolution images, several hundred NPs), 76 Ag NPs with good orientation and focus, which were classified into the three possible structures according to their prevalence. Most of the nanocrystals obtained from **1** and **2** are polycrystalline. Fig. 2a-e shows examples of identifiable images of multiple-twinned nanoparticles (*Ih*, Fig. 2a-c, *D*5*h*, Fig. 2d) and *FCC* ones (Fig. 2e). An equivalent set of around 1080 nanocrystals form a regular pavement on amorphous carbon spanning over $10^{-2}\mu m^2$ (see Fig. S4 in the Supporting Information, Section 1). According to our statistics (Fig. 2f), only one nanocrystal presents a *FCC* structure (1 %), 6 being *D*5*h* (8 %) and 69 being *Ih* (91 %). Hence the *Ih* nanocrystals are clearly the dominating forms, as suggested also by the well defined (111) planes over (200) ones displayed by X-ray diffraction patterns of Ag NPs (see Fig. S3, Supporting Information, Section 1).

The quasi-absence of *FCC* nanoparticles at the detected size (6.2–6.9 nm) in this work is counter-intuitive, since previous studies of Ag NPs chemically synthesized from $AgNO_3$ precursor [29,35,44,45], and especially with formamidinate [45] or hexadecylamine capping agents [26,29,35], have identified the *FCC* morphology from X-Ray diffraction or transmission electron microscopy in the range 1–24 nm. [26,29,35,44,45] Our results are in better correspondence with those related to chemically synthesized Ag NPs from $AgNO_3$ precursor with other capping ligands than amine or amidine, such as polyvinylpyrrolidone, [33,34,37,41] citrate [37] or tartrate [39], for which the icosahedral symmetry is prevalent.

Multiscale theoretical modeling

In order to understand the very low statistics of *FCC* clusters, a DFT modeling of Ag NPs interacting with methyl amidine **mAMD** and model ligands of **HDA** (for instance octylamine **OTA**) is exposed in the following (see Materials and Methods and Supporting Information, Section 2). Since the synthesis environment of Ag NPs is rather complex with the contributions of ligands chemistry, solvent, support, temperature and pressure, and due to the clear lack of related theoretical modeling in the literature, we have developed several atomistic models aiming to disentangle all these effects. We have considered various high symmetry Ag NPs and different orientations of Ag extended surfaces. Different DFT functionals including weak van der Waals interactions

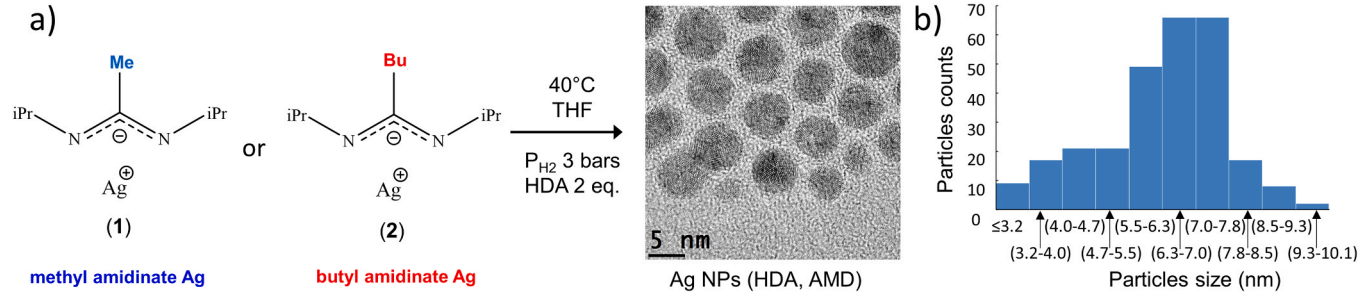

Fig. 1. (a) Scheme showing the synthesis of silver nanoparticles from the silver amidinate precursors (**1** namely N,N'-diisopropylacetamidinate silver(I) referred to as methyl amidinate Ag, and **2** namely N-N'-diisopropyl-n-butylamidinate silver(I) referred to as butyl amidinate Ag), in tetrahydrofuran (THF) under moderate temperature and H_2 pressure. Silver nanoparticles, which are stabilized by amidine (**AMD**) coming from the precursor hydrogenolysis and hexadecylamine (**HDA**), are illustrated by a HRTEM image of ligand-capped Ag nanoparticles. (b) Histogram of nanoparticle size distribution resulting from precursor **1** with an average diameter of 6.2 nm and a standard deviation of 1.4 nm (see the histogram of precursor **2** in Fig. S2b of the Supporting Information, Section 1).

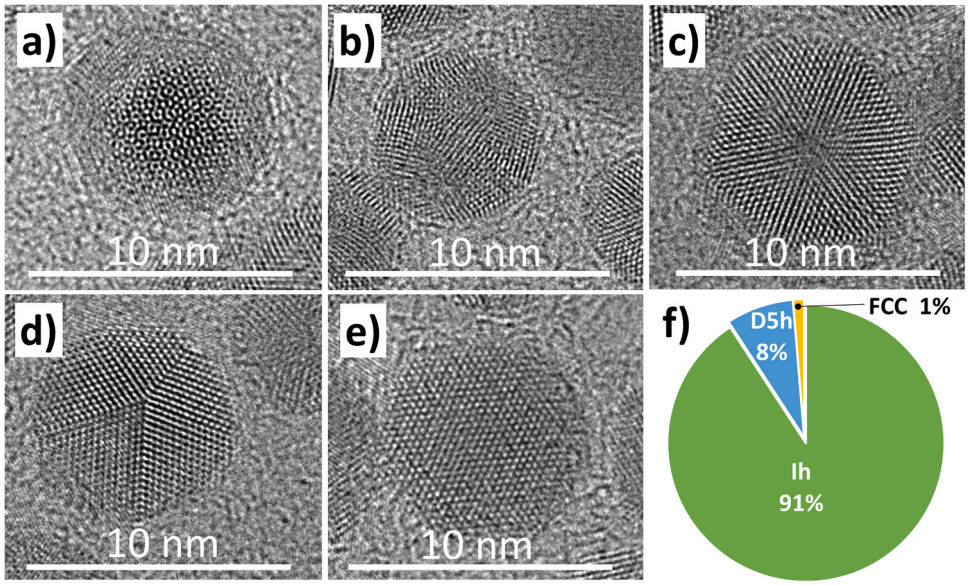

Fig. 2. Selected HRTEM images of different Ag NPs morphologies present on the amorphous carbon support: a-c) three different possible orientations and tilting angle of *Ih* nanocrystals, d) *D*5*h* and e) *FCC* NPs and f) distribution statistics of Ag NPs symmetries.

have been used. Our theoretical results do not depend on the choice of the DFT functional (Tables S1-S8, Supporting Information, Section 3).

Synthesis energy

In the following, we have formalized the experimental synthesis protocol by a global chemical equation (see Eq. (1)), useful for the theoretical modeling to define the synthesis energy noted Γ_{syn} and normalized by the surface area (nanoparticle or extended surface).

$$p[M_xL_y] + p'[M_{x'}L'_{y'}] + S \underset{\text{medium}}{\overset{\Gamma_{syn}}{\rightarrow}} M_NL_lL'_{l'}S + (py - l)L + (p'y' - l')L' \quad (1)$$

$$N = px + p'x'; l \le py; l' \le p'y' \quad (2)$$

$$\frac{p}{2}[Ag_2(OTA)_2] + \frac{p'}{2}[Ag_2(mAMD)_2] + Gr \underset{\text{medium}}{\overset{\Gamma_{syn}}{\rightarrow}} Ag_N(OTA)_l(mAMD)_{l'}Gr + (p - l)OTA + (p' - l')mAMD \quad (3)$$

$$N = p + p'; l \le p; l' \le p' \quad (4)$$

$$\frac{p}{2}[Ag_2(OTA)_2] + \frac{p'}{2}[Ag_2(mAMD)_2] \underset{\text{medium}}{\overset{\Gamma_{diss}}{\rightarrow}} NAg + (p)OTA + (p')mAMD \quad (5)$$

$$NAg \underset{\text{medium}}{\overset{\Gamma_{coh}}{\rightarrow}} Ag_N \quad (6)$$

$$Ag_N + (p)OTA + (p')mAMD \underset{\text{medium}}{\overset{\Gamma_{coads}}{\rightarrow}} Ag_N(OTA)_l(mAMD)_{l'} + (p - l)OTA + (p' - l')mAMD \quad (7)$$

$$Ag_N(OTA)_l(mAMD)_{l'} + Gr \underset{\text{medium}}{\overset{\Gamma_{adh}}{\rightarrow}} Ag_N(OTA)_l(mAMD)_{l'}Gr \quad (8)$$

In this equation, the formation of metallic NPs M_N (N being the total number of metallic atoms, corresponding to N_{SA} - for silver atoms as defined in the Supporting Information, Section 2) functionalized by ligands L and L', and deposited on a support S, in the context of a medium (gas, solvent), results from the complete decomposition of two metallic precursors M_xL_y and $M_{x'}L'_{y'}$ yielding isolated M atoms and ligands L and L'. If we apply this model in our context of Ag NPs functionalized by **OTA** and **mAMD** ligands and supported on graphite Gr, one can decompose the global balance (Γ_{syn}, Eq. (3) and Eq. S11, Supporting Information, Section 2) in four chemical subequations (Eq. S12a, Supporting Information, Section 2) describing in turn the precursor complete dissociation (Γ_{diss}, Eq. (5) and Eq. S12b, Supporting Information, Section 2), the clean Ag NP formation (Γ_{coh}, Eq. (6) and Eq. S12c, Supporting Information, Section 2), the ligand coadsorption at the surface of the Ag NP (Γ_{coads}, Eq. (7) and Eq. S12d, Supporting Information, Section 2) and the adhesion of the complete functionalized Ag NP on graphite (Γ_{adh}, Eq. (8) and Eq. S12e, Supporting Information, Section 2), respectively. Note that in these equations, the structure of the metallic nanoparticle can be crystalline, non-crystalline, amorphous, defective, or truncated.

Small Ag NPs DFT models

A direct exploration through *ab initio* models is out of reach at the targeted experimental size of 6.2–6.9 nm. In addition, the investigation of ligand adsorption requires a large number of configurations which is also unachievable for large-sized clusters. This justifies our strategy to start with DFT models of small silver nanoclusters in the range 54–79 atoms (around 1.5 nm) in interaction with specific ligands (see Fig. 3a-d and Supporting Information, Section 3.1). In order to represent the detected symmetries in competition, four clusters of different morphologies have been selected: regular decahedral Ag54deca (*D*5*h*), Mackay icosahedral Ag55ico (*Ih*), Marks-decahedral Ag75marks (*D*5*h*) and irregular truncated octahedral Ag79ito (*Oh*). Complementary tests have been done for ino decahedral Ag55ino (*D*5*h*) and cuboctahedral Ag55cubo (*Oh*) which correspond to local minima in absence of ligands. For **HDA**, the most simplified ligand model is butylamine (C4 aliphatic chain, noted **BTA**). Numerous top monoadsorption forms (usually named $\eta_1\mu_1$) have been optimized on these small clusters and the most stable structures have been further optimized by considering an amine ligand with a longer aliphatic C8 chain, octylamine noted **OTA** (see Tables S1-S3 and Fig. S6-S9 in the Supporting Information, Section 3). A moderate adsorption strength is found for **BTA** (0.78–0.91 eV.molec^{-1}) and **OTA** (0.90–1.32 eV.molec^{-1}) in agreement with a previous DFT study of cysteine amino acid on small Ag clusters [64] showing a preferential bonding through the amino group, but also with previous trends of amino acids interacting with silver predicted by combined INTERFACE/CHARMM36 force fields. [77] Note that, throughout the study, the adsorption energetics is dominated by the van der Waals interactions. Then adsorption models at saturation for **BTA** have been developed by considering its most stable adsorption positions, and for **OTA**, the saturation models have been optimized by extending the chain

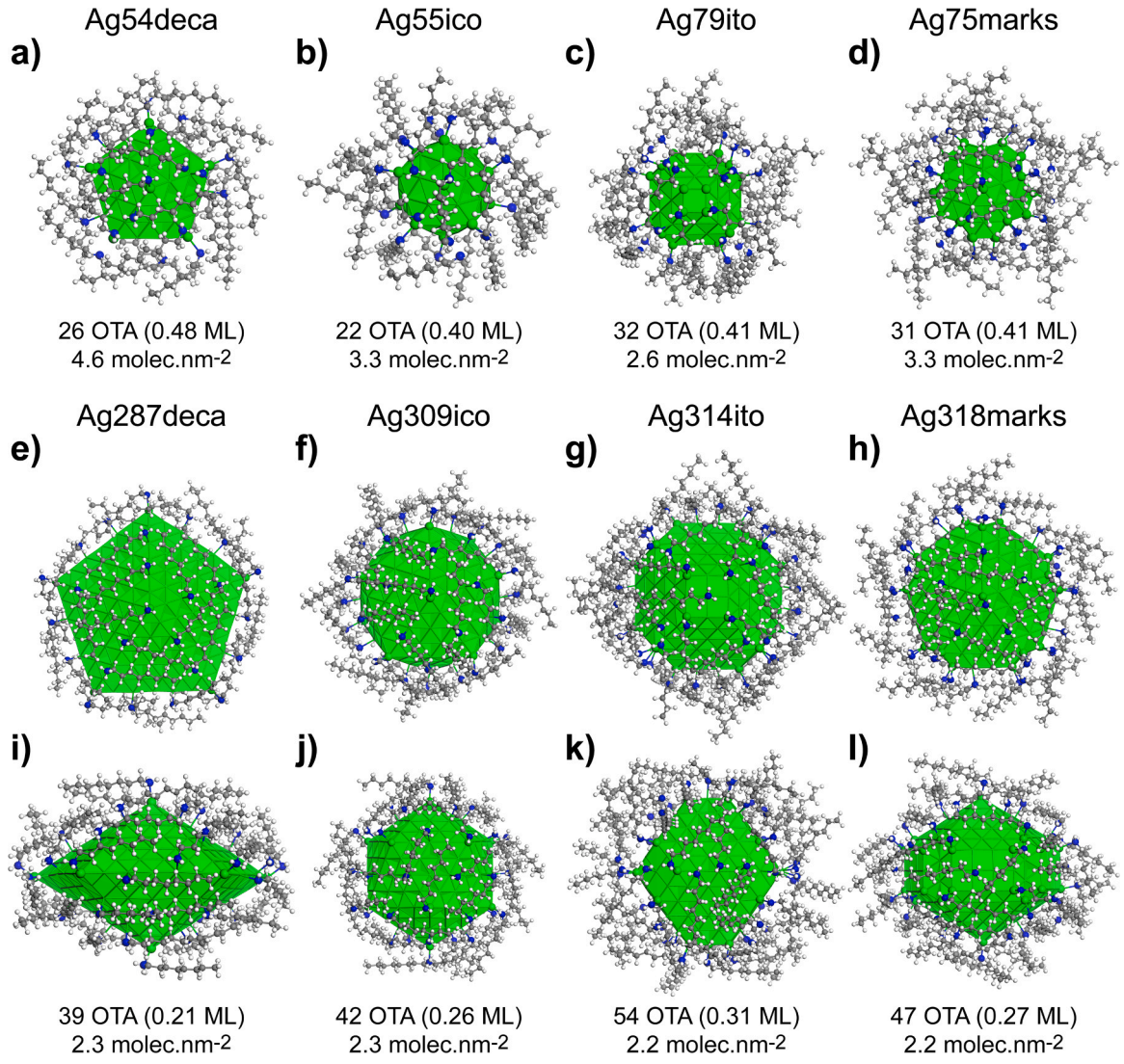

Fig. 3. Top views of optimized structures (DFT models) of functionalized small Ag NPs (54–79 atoms, 1.5 nm) by monoshells of octylamine (**OTA**) ligands: a) regular decahedral Ag54deca, b) Mackay icosahedral Ag55ico, c) irregular truncated octahedral Ag79ito, d) Marks-decahedral Ag75marks. Top and lateral views of optimized structures (DFT models) of functionalized larger Ag NPs (287–318 atoms, 2.5 nm) by monoshells of **OTA** adsorbates: e,i) regular decahedral Ag287deca, f,j) Mackay icosahedral Ag309ico, g,k) irregular truncated octahedral Ag314ito and h,l) Marks-decahedral Ag318marks. Corresponding number of adsorbed **OTA** ligands (coverage, ML = monolayer) and molecule surface density MSD (molec.nm^{-2}). The color label is green for silver, blue for nitrogen, grey for carbon and white for hydrogen atoms. The vertices of the Ag NPs are represented by balls, whereas the bonds between surface Ag atoms are depicted by joint sticks. Core Ag atoms appear with solid representation.

lengths of the **BTA** corresponding models (see Fig. 3a-d for adsorption at saturation; see Tables S1-S3 and Fig. S13-S14, Supporting Information, Section 3). The effect of coverage is presented in Fig. 4a for **OTA** and in Fig. S5 of the Supporting Information (Section 3). The stability of the ligand-covered silver nanoclusters is captured by the DFT synthesis energy Γ_{syn} (Eq. (3) and Eq. S9, Supporting Information, Section 2), which is plotted as a function of the molecule surface density MSD (Eq. S1, Supporting Information, Section 2). For the case of amidinate synthesis precursors, the methyl amidine molecule, noted **mAMD** throughout the study, has been chosen for DFT monoadsorption and saturation models, by following an approach similar to the one used for **BTA** (see Tables S4-S6 and Fig. S10-S12, S15 of the Supporting Information, Section 3). According to this preliminary study, **BTA** and **OTA** are related to a more exothermic Γ_{syn} (for example −60.9 and −61.3 meV.Å^{-2} on Ag54deca for **BTA** and **OTA**, respectively) than **mAMD** (-53.8 meV.Å^{-2} on Ag54deca), whatever the nanocluster model, thus meaning a preference for **OTA**. This has also been confirmed on the Ag(111) surface by exploring the relative stability of **OTA** and **mAMD** monoadsorption from a combination of DFT calculations and *ab initio* molecular dynamics (Supporting Information, Section 9). Mixed coadsorption models at saturation have thus been developed by considering a large excess of **OTA** over **mAMD** (see Table S7 and Fig. S16 of the Supporting Information, Section 3). The first key theoretical result shows that the decahedral Ag54deca is always the most stable one among the four considered small nanoclusters, whatever the composition of the ligand shell at saturation. This is illustrated in Fig. 4a in the case of **OTA**. The icosahedral Ag55ico and Marks-decahedral Ag75marks offer an intermediate stability between Ag54deca and the irregular truncated octahedral Ag79ito. To ensure that no other competitive morphology could be more favorable than the regular decahedral symmetry (Ag54deca), Ag55cubo and Ag55ino covered by a shell of **OTA** ligands at saturation have also been optimized in similar computational conditions. Both systems have entirely transformed into Ag55ico or Ag55twin, respectively (see Table S2 and Fig. S14 of the Supporting Information, Section 3), without desorbing any **OTA** ligand during the geometry optimizations. Moreover, the theoretical stability

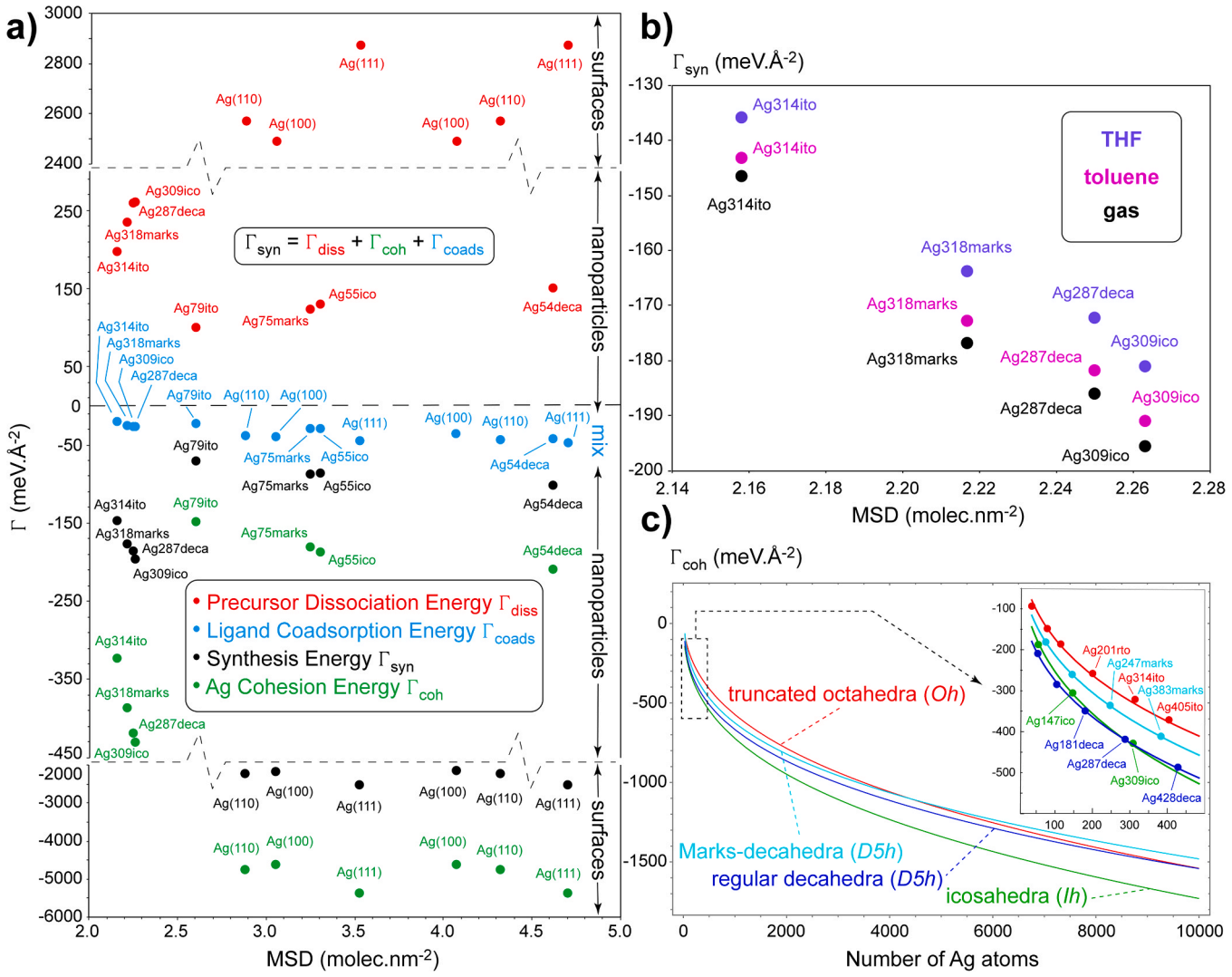

Fig. 4. a) DFT models. Synthesis energy Γ_{syn} (black points, meV.Å^{-2}) against molecule surface density (MSD, molec.nm^{-2}) for Ag NPs (54–318 atoms) and extended flat surfaces (111), (100), (110) covered by octylamine (**OTA**) ligands in vacuum and decomposed into three components: dissociation energy of the silver precursor Γ_{diss} (red points), cohesion energy of clean Ag NPs and surfaces Γ_{coh} (green points) and ligand coadsorption energy Γ_{coads} (blue points). Note that all energies Γ are normalized to surface area, either of the nanoparticle or of the surface. The definition of each Ag nanoparticle or surface is indicated close to its corresponding point. b) DFT models. Solvent effects (THF, purple points and toluene, pink points) on Γ_{syn} for Ag NPs (287–318 atoms) compared to gas phase systems (black points). c) Mathematical model based on DFT data of Ag NPs and surfaces. Γ_{coh} (Eq. (9)) of the four key morphological families of Ag NPs (defined by four different colors) plotted as a function of the total number of Ag atoms up to 10000 atoms (corresponding to a diameter D of 8 nm according to the formula $D = 0.371 \times N^{1/3}$, where the nanoparticle volume is approximated as the one of a sphere). In the range 50–450 atoms, an insert displays the region where regular decahedra and icosahedra are competitive (crossing point at 285 atoms).

order in favor of Ag54deca does not depend on the MSD in **OTA** or **mAMD** (see Fig. S5 of the Supporting Information, Section 3). Hence, our conclusions at small sizes (54–79 atoms) disagree with our measurements in the range 6.2–6.9 nm. This questions the relevance of the chosen size for interpreting experiments.

Nanoparticle size effects

In order to evaluate the influence of the nanoparticle size on the competition between the concerned morphologies, DFT models of larger size nanoparticles in the range 287–318 atoms (around 2.5 nm) have been investigated by considering decahedral Ag287deca, icosahedral Ag309ico, irregular truncated octahedral Ag314ito and Marks-decahedral Ag318marks nanoparticles covered by monoshells of ligands in vacuum (see Fig. S17 in the Supporting Information, Section 3.2). Thanks to the analysis at small size with Γ_{syn}, highlighting the preference of **OTA** adsorbate over **mAMD**, only pure monoshells of **OTA** have been developed in the models at large size (Fig. 3e-l for the optimized structures). The number of **OTA** molecules (from 39, in the case of Ag287deca, to 54 ligands, for Ag314ito) has been chosen to obtain quasi-identical MSD for all morphologies (2.2–2.3 molec.nm^{-2}), and leading to a narrow range of coverage (0.21–0.31 ML). Such a change in the number of ligands is due to the large difference of accessible Ag NP surface area; the lowest area being calculated for Ag287deca and the largest one for Ag314ito (Table S8, Supporting Information, Section 3). The starting configuration and conformation of the monoshells use the conclusions of the previous models at small size: top adsorption for **OTA** adsorbed on nanoparticle kinks, edges and facets, and minimization of steric repulsions between molecules by assembling them in parallel patterns. All along the geometry optimizations, no desorption has been registered, thus meaning that the chosen MSD are below saturation. As shown in Fig. 3e-l, the optimal structures of coadsorbed ligands show clear discrepancies. The **OTA**-covered icosahedral and decahedral Ag NPs present much more organized ligand shells than the truncated octahedral nanoparticle. In the case of

Ag309ico, the self-assembly of **OTA** ligands leads to a homogeneous coating at the nanocluster surface, mimicking a spherical "wool ball". For the decahedral Ag287deca and Ag318marks, the self organization of **OTA** ligands follows a motif resembling a "regular hair" wrapping around the *C5* symmetry axis of the decahedra. The main difference between decahedra appears in the interaction of the **OTA** ligand with the Ag NPs. For Ag287deca, the envelope of the **OTA** molecules is more convex thanks to van der Waals interactions with the Ag NP edges, whereas for Ag318marks, the ligand hull exhibits weaker interactions between the ligand octyl moieties and the Ag NP facets presenting (110) concavities and (100) orientations. In the case of Ag314ito, the ligand coating is strongly disorganized and inhomogeneous. Concerning now the stability order, Γ_{syn} is calculated as for small Ag NPs and plotted in Fig. 4a (see Table S8 in the Supporting Information, Section 3). Interestingly, at larger size, the stability order matches experimental conclusions as follows: Ag309ico being more stable than Ag287deca and Ag318marks, Ag314ito being the least stable nanoparticle (Fig. 4b). Hence when the nanoparticle size increases from 50 to 300 atoms, the icosahedral symmetry becomes preferential over the decahedral one. Note the least stability of *FCC* symmetry whatever the size, in agreement with measurements.

We investigate in more details the various contributions (Γ_{diss}, Γ_{coh} and Γ_{coads}) included in the synthesis energy Γ_{syn}, as previously introduced (Eq. (5)-(7) and Eq. S9-S10(a-d), Supporting Information, Section 2). All these contributions are normalized by the nanoparticle surface area, so as Γ_{syn} is linked to them by an additive model, and plotted against MSD (Fig. 4a and Table S9 in the Supporting Information, Section 3). By crossing all the nanoparticle sizes from 54 to 318 atoms, the DFT calculations show that the ligand coadsorption energy (negative and stabilizing component) is always really minority and quasi-constant when MSD changes, whereas the Ag cohesion energy (negative and stabilizing component) is by far the major contribution to the synthesis energy. Surprisingly, the latter captures almost linearly the variations of the synthesis energy, thus meaning that the only knowledge of Ag cohesion energy normalized to the nanoparticle surface area is enough to predict the stability order between Ag nanoparticles. Indeed, the precursor dissociation energy, which is a positive and destabilizing contribution, is always secondary in the additive model. A minor remark concerns the weak increase of adsorption strength of **OTA** as MSD increases, due to stabilizing lateral van der Waals interactions predominant over steric hindrance.

Although predictive with respect to experiments, the previous atomistic DFT models of Ag NPs around 2.5 nm are not enough to allow a direct comparison with measurements at 6.2–6.9 nm. Since the Ag cohesion energy normalized to surface area leads the overall stability order, one can check this trend at another extreme size limit by developing DFT models representative of very large size nanoparticles (infinite facets). To do so, self-assembly models (SAM) of **OTA** on Ag (111), (100) and (110) extended surfaces have been built and optimized with DFT by considering two different coverages close to saturation (see Table S14 and Fig. S23-S25 in the Supporting Information, Section 6). According to computed energetics (Fig. 4a), in the explored range of MSD (≈3–5 molec.nm^{-2}), the coadsorption energy Γ_{coads} is minority and follows the previous trend observed for Ag NPs. The SAM stability order shows that Ag(111) is the most stable surface whatever MSD, and the Ag cohesion energy Γ_{coh} rules the stability order, likewise for Ag NPs. In summary for the SAM, in agreement with experiments, the dense Ag (111) surface outperforms the more open Ag(100) and Ag(110) terminations, thus confirming the clear preference for (111) orientations demonstrated previously for large size *Ih* Ag NPs.

Multiscale mathematical model

Thanks now to the complementary DFT predictions at small size (Ag NPs) and infinite size (Ag extended surfaces), one can develop a multiscale mathematical model bridging these extreme size limits, by considering a continuous approach describing the variations of the clean Ag nanoparticle cohesion energy normalized by its surface area as a function of the number of Ag atoms:

$$\Gamma_{coh} = \Gamma_{coh0} + \widetilde{\Gamma}_{coh1}\left(G(s_{edge})\right)^{1/3} \quad (9)$$

where G is the total number of Ag atoms for a given morphology (Table S19, Supporting Information, Section 8), s_{edge} being the number of Ag atoms belonging to one edge of the nanoparticle (see Fig. 4a for the different contributions to the synthesis energy, Fig. 4c for results of the mathematical model and in the Supporting Information (Section 8), for the development of the model). The offset and the slope noted Γ_{coh0} and $\widetilde{\Gamma}_{coh1}$, respectively, are computed on the basis of DFT calculations for Ag (111), (100) and (110) extended surfaces and a large series of Ag NPs in the range 38–1415 atoms, for four different morphologies including truncated octahedra, icosahedra, regular and Marks decahedra (Table S18, Supporting Information, Section 8). This mathematical model predicts a clear preference of icosahedral symmetry over regular or Marks-decahedral morphologies in the range 250–10,000 atoms, and especially at the targeted experimental size. This means that *Ih* symmetry is always favored in a large range of sizes over all the other morphologies, in striking agreement with experiments. At small sizes (below 285 atoms), the continuous mathematical model reconciles also with atomistic DFT predictions, since the regular decahedral symmetry becomes the most stable one (see insert in Fig. 4c and Fig. S27 of the Supporting Information, Section 8). Besides, at very large size (above 1 million of Ag atoms or an approximate diameter of 30 nm), it predicts that the *FCC* symmetry, which is never competitive in a very large range of sizes, becomes finally the most stable one, as expected for a *FCC* metal. The cohesive energy normalized to the nanoparticle surface area thus appears as a useful descriptor for capturing relevantly the stability order between the classical morphologies of Ag NPs. Our central idea is compatible with previous considerations stating that the atomic cohesive energy determines the thermodynamic performance of materials through atomic coordination changes. [85]

Solvent effects

An important element of the chemical environment is the solvent which has been neglected so far in the theoretical modeling. Although difficult to describe from an explicit standpoint due to the large size of the systems (ligand-covered Ag NPs and tetrahydrofuran, THF or toluene solvent molecules), solvent effects can be modeled from an implicit approach such as the polarizable continuum model, implemented in DFT (Supporting Information, Section 4). In this work, all the previously exposed DFT models of ligand-covered Ag NPs have been reoptimized in toluene and THF by considering monoshells of **OTA**, of **mAMD** and of coadsorbed **OTA** and **mAMD** for small size NPs in the range 54–79 atoms (see Table S10 and Fig. S18 in the Supporting Information, Section 4), and monoshells of **OTA** for large size NPs in the range 287–318 atoms (Fig. 4b and Table S11 in the Supporting Information, Section 4). Whatever the size range, the solvent effects change neither the optimal structures of ligand-covered Ag NPs nor the conclusions drawn in vacuum which state that the decahedral Ag54deca cluster is preferential at small size, whereas the icosahedral Ag309ico is the most stable nanoparticle at large size. The solvents modify neither the stability order between the NPs morphologies nor the one between **OTA** and **mAMD** ligands. As shown in Fig. 4b (Fig. S18 in the Supporting Information, Section 4), the solvents tend to systematically destabilize the ligand-covered Ag NPs with a slighter effect for toluene.

Support effects

Another important element of the characterization environment is the presence of the amorphous carbon support, which has been chosen experimentally, as it is assumed chemically inert. Such assumption has been investigated in this work, by describing the support effects with a graphite surface model, at the DFT level (see Fig. 5a-b and Supporting Information, Section 5). In order to maximize them, we have chosen to

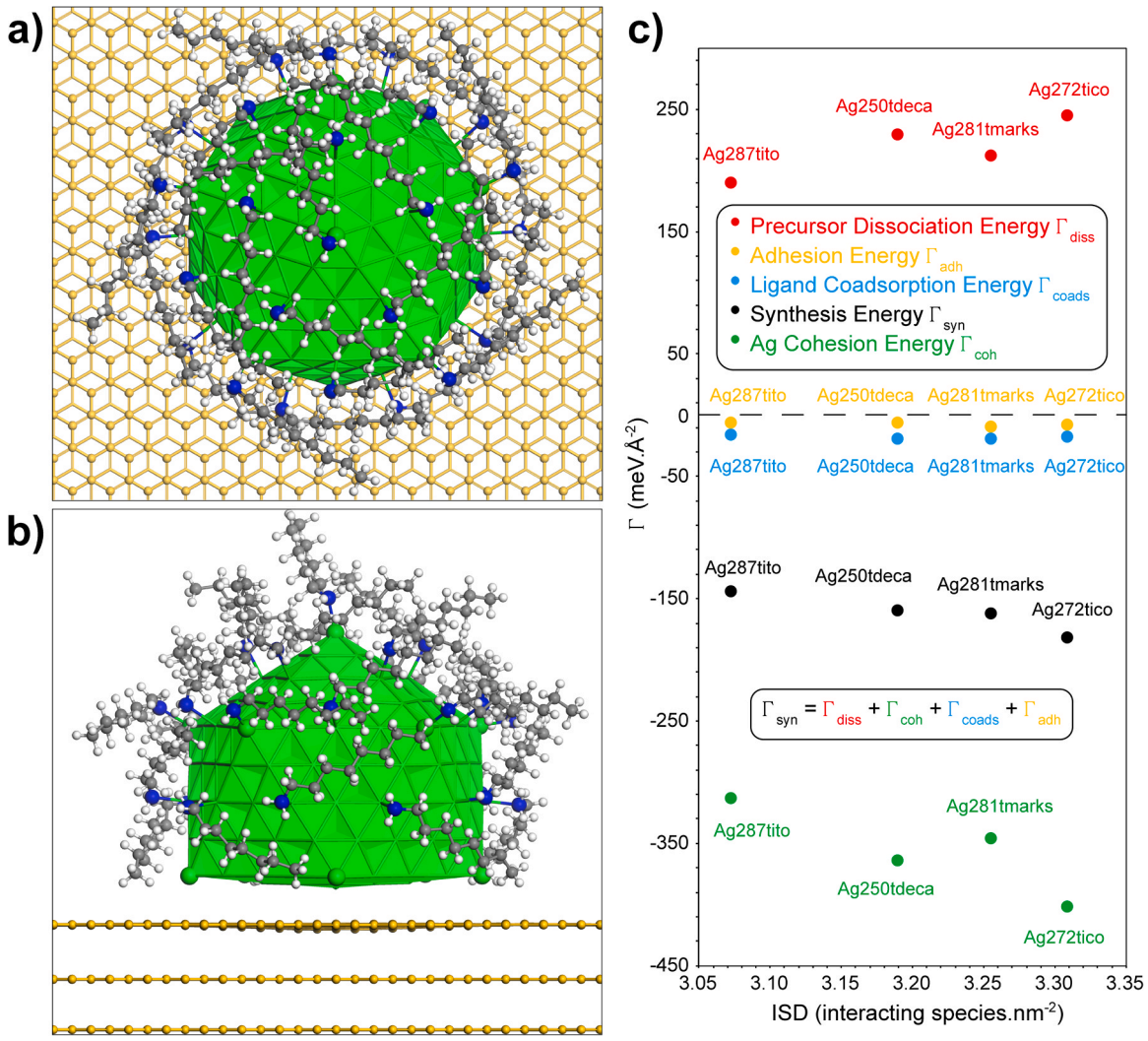

Fig. 5. Top a) and lateral b) views of the optimized structure (DFT model) of a truncated icosahedral Ag272tico nanoparticle covered by 26 octylamine ligands and supported on a graphite (0001) surface (trilayer slab and (16 × 16) supercell). The color labels are yellow for carbon atoms of graphite, green for silver, gray for carbon atoms of ligands, blue for nitrogen and white for hydrogen. Ag atoms belonging to vertices, C atoms belonging to the surface layer of graphite and to ligands, N and H atoms are all represented by balls, while Ag atoms of edges and facets are marked by joint sticks. C atoms belonging to subsurface layers of graphite are marked by balls in a) and by joint sticks in b). Ag atoms of NP core are depicted by solid representation. c) DFT models. Synthesis energy Γ_{syn} (black points, meV.Å^{-2}) against interacting species density (ISD, interacting species.nm^{-2} corresponding to either octylamine ligands or silver atoms bound to graphite) for truncated Ag NPs (250–287 atoms) covered by octylamine ligands in vacuum, supported on a graphite (0001) support and decomposed into four components: dissociation energy of the silver precursor Γ_{diss} (red points), cohesion energy of clean Ag NPs Γ_{coh} (green points), ligand coadsorption energy Γ_{coads} (blue points) and adhesion energy on support Γ_{adh} (yellow points). Note that all energies Γ are normalized to NP surface area. The definition of each Ag NP is indicated close to its corresponding point.

generate massive defects by truncating the Ag NPs in the range 287–318 atoms and interfacing the resulting facets with graphite (0001). These defects lead to the truncated decahedron Ag250tdeca (resulting from Ag287deca), truncated icosahedron Ag272tico (obtained from Ag309ico), truncated Marks decahedron Ag281tmarks (built from Ag318marks) and truncated irregular octahedron Ag287tito (modeled from Ag314ito) (see Tables S12-S13 and Fig. S19-S22 in the Supporting Information, Section 5). The highly unsaturated Ag surface atoms of truncated facets are expected to bind more strongly to graphite by comparison with regular surface atoms. Moreover, the truncations have been made to create flat facets of equivalent silver atom interface density, from 8.59 to 10.90 at.nm^{-2} (Table S12, Supporting Information, Section 5), not to bias the conclusions. The adhesion energy on graphite, from −0.25 to −0.43 eV per silver interface atom, is in fair agreement with a recent theoretical study devoted to the deposit of Ag_{20} cluster on graphene (-0.371 eV per Ag atom). [86] Concerning the choice of the **OTA** adsorption monoshells, the structures previously optimized in vacuum have been used (Fig. 3e-l). In order to keep maximal the interactions between truncated Ag NPs and graphite, **OTA** ligands have not been kept in between the metal and the support. However, they could decorate laterally the boundary between them. The stability order between supported defective nanoclusters has been evaluated by plotting the synthesis energy Γ_{syn} (Eq. (3) and Eq. S11, Supporting Information, Section 2) normalized to the total truncated Ag NP surface area (Fig. 5c), as a function of the interacting species density (ISD, Eq. S2, Supporting Information, Section 2). The DFT calculations show that neither the support nor the defects modify the previous conclusions. The truncated icosahedron Ag272tico is the most stable nanoparticle, while the truncated irregular octahedron Ag287tito remains the least stable one (the two truncated decahedra being intermediate with a comparable stability). Hence our most realistic DFT models agree with experimental observations. The energy decomposition analysis of Γ_{syn} can be derived by extending the previous decomposition model with a fourth term noted Γ_{adh} and corresponding to the adhesion energy on support (Eq. (3)-(8) and Eq. S11-S12(a-e), Supporting Information, Section 2). The final conclusions drawn from this more complete model are identical to

the ones evoked previously. The stabilizing Ag cohesion energy remains the predominant contribution, while the destabilizing precursor dissociation energy is secondary and the stabilizing ligand coadsorption energy is minority and constant. The stabilizing adhesion energy of the ligand-covered Ag NPs on graphite is the smallest contribution and is also constant between considered morphologies. This confirms our experimental hypothesis regarding negligible support effects and shows original results with respect to a previous investigation of Ag NPs supported on silica, where the position of the crossover points between morphologies was found sensitive to the physical nature of the support. [16]

Conclusion

In summary, we have synthesized silver nanoparticles from two silver amidinate organometallic precursors and hexadecylamine ligands solvated in organic solvents. At the targeted size (6–7 nm) of Ag NPs, a counter-intuitive result is found from HRTEM measurements showing a quasi-absence of the *FCC* structure in the statistics of the ordered nanoparticles. A large majority of icosahedral nanoparticles (*Ih*) has been registered with a minor set of decahedral clusters (*D5h*). To interpret such an unexpected trend, energetics of DFT models of Ag NPs in the range 1.5–2.5 nm (54–318 atoms) and of extended Ag surfaces has been used to develop a multiscale approach predicting the stability order of the competitive morphologies at the experimental size. Various elements of synthesis environment have been described in the DFT models either by an explicit approach (amine ligands, support effects) or by an implicit model (solvent effects). An original descriptor, named synthesis energy, has been introduced and decomposed into several energetic contributions. Among them, the clean nanoparticle cohesion energy normalized by its surface area appears as the prevalent component. A mathematical function fitting the DFT data related to ordered nanoparticles is used to predict the morphological competition at any size. Since we consider moderately-bound ligands, the contribution of the normalized adsorption energy to the synthesis energy remains minority. In agreement with our experiments, theoretical models of large size ligand-covered Ag NPs predict a superior stability of the icosahedral symmetry up to very large sizes (30 nm, 1.000.000 atoms). As expected, for even larger nanoparticles, the *FCC* symmetry becomes more stable. Defects of Ag NPs, solvent and support effects do not alter these conclusions. Thanks to the validation with measurements, the multiscale modeling demonstrates that the normalized cohesion energy of clean Ag NPs is a relevant descriptor for capturing stability order. The role of ligands appears indirectly in this descriptor through the accessible nanoparticle surface area. The robustness of our theoretical multiscale approach combining *ab initio* models at various sizes and continuous mathematical models opens very promising perspectives for determining the stability order of other functionalized metallic nanoparticles and related morphologies in complex synthesis environment, where the relative weights of the various contributions of the synthesis energy may change. This study paves the way to the investigation of other complex properties of functionalized metallic nanoparticles, such as their dynamic response toward temperature and pressure.

Materials and methods

Colloidal Ag NPs synthesis

In a glove box, silver precursor (0.22 mmol) was weighed and introduced in a Fisher Porter (FP) reactor and dissolved in THF (3 ML). The **HDA** ligands were separately weighed (0.44 mmol) and added to the silver precursor solution, synthesized by following a previous protocol. The FP reactor was placed on an argon/vacuum vessel and pressurized with H_2 (3 bar). The reactor was then placed into an oil bath at moderate temperature (40°C) and let for the night. Yellow colloidal solutions of Ag NPs are obtained after 12 h. Precursor **1** (methyl amidinate) consists in a 3.6:1 ratio of dimer and trimer silver amidinate molecule. Interestingly, precursor **2** (butyl amidinate) crystallizes as a tetramer which only slowly dissolves in THF whilst transforming into dimer and trimer species in solution. The final ratio of each species is driven by the concentration of the precursor in the solvent. During the hydrogenolysis of the precursor, the amidine moieties (methyl or butyl amidine) are released in the solution and actively participate to the stabilization of Ag NPs. The added **HDA** ligand also participates to the NPs stabilization.

Transmission electron microscopy

TEM grids were prepared in a glove box under argon atmosphere by depositing a drop of colloidal Ag solution onto a copper grid with a thin carbon layer. The TEM experiments were performed on a JEOL JEM 1400, Tokyo, Japan transmission electron microscope operating at 120 kV with a resolution of 2.04 Å.

High resolution transmission electron microscopy

HRTEM analysis was carried out both on JEOL JEM 2100 F field emission gun transmission electron microscope (FEG-TEM) operating at 200 kV with a resolution of 2.3 Å (point-point) and 1 Å (line), and on a JEOL JEM-ARM200F Cold FEG-TEM with a resolution image of 1.9 Å point.

Computational details

DFT calculations were performed by using the VASP code [87–89] together with the PBE-D3 semi-empirical dispersion-corrected functional in its zero-damping formalism (PBE-D3(0D)) [90]. The interactions between electrons and ion cores were described by PAW potentials [91] and valence electrons by plane wave basis sets in tight conditions (with a kinetic cutoff energy of 400 eV). For the DFT models of Ag nanoparticles, a large simulation box ($50 \times 50 \times 50$) $Å^3$ was used in order to ensure a large vacuum space between periodically equivalent systems. The Brillouin zone sampling in reciprocal space corresponds to the Γ point. For the Ag extended surfaces, the k-point meshes were selected accordingly: on Ag(111), ($21 \times 21 \times 1$) for the $(\sqrt{3} \times \sqrt{3})$R30° and ($19 \times 19 \times 1$) for the ($2 \times 2$) supercells; on Ag(100), ($17 \times 27 \times 1$) for the $(\sqrt{5} \times \sqrt{2})$R108° and ($19 \times 19 \times 1$) for the ($2 \times 2$) supercells; on Ag(110), ($21 \times 21 \times 1$) for the $(\sqrt{3} \times \sqrt{3})$R109° and ($15 \times 21 \times 1$) for the $(\sqrt{6} \times \sqrt{3})$R90° supercells. For the bulk of graphite, the tight convergence of total electronic energy has been reached with a ($22 \times 22 \times 8$) k-point mesh. The corresponding volume has then been optimized with this k-point grid at the PBE-D3(0D) level. For the DFT models of Ag NPs supported on the graphite (0001) surface (the graphite slab being composed of 3 layers), the Brillouin zone sampling in reciprocal space has been restricted to the Γ point, due to the considered very large (16×16) supercell. The implicit solvation effects were evaluated by using VASPsol [92–94], a software package that incorporates solvation into VASP within a self-consistent continuum model. All the degrees of freedom of all atoms in the chemical systems were relaxed during the geometry optimizations, with a tight convergence criterion of 10^{-6} eV for the total electronic energy, until each residual force on nuclei was less than $\pm$ 0.01 eV.$Å^{-1}$. For the graphitic systems, the geometry of the two bottom layers was kept frozen at the optimized bulk situation, whereas the top layer of graphite was totally relaxed, as well as all the degrees of freedom of the supported and functionalized Ag NPs, with identical convergence criteria (10^{-6} eV and $\pm$ 0.01 eV.$Å^{-1}$).

More details about the experimental and theoretical methods are exposed in the Supporting Information (Sections 1 and 2).

Funding

This study was supported by the CPER/SYSPROD 2015–2022 contract (N°2019-AURA-P5B) and AXELERA Pôle de Compétitivité (PSMN Data Center).

Author statement

DL and NT have conceived the theoretical project (ideas, formulas, goals and aims), built, performed and analyzed all the DFT models and calculations, elaborated the methodology of the multiscale modeling and the development of the related software in Mathematica, managed the computational resources and the funding acquisition (DL), as well as the writing of the original draft (including visualization and generation of all the theoretical graphics), its reviewing and editing. They have participated to the scientific working meetings.

PF has conceived the experimental project, carried out the synthesis, the characterizations and the analysis, as well as the writing of the original draft (including visualization and generation of all the experimental graphics), its reviewing and editing. He has participated to the scientific working meetings.

CL-D, FR, KF and MK have participated to the improvement of the original draft and its editing, as well as to the scientific working meetings.

CL has initiated the collaboration, organized and animated the working meetings. She has managed a part of the CALMIP computational resources and participated to the improvement of the original draft and its editing.

VC has contributed to the experimental characterizations and analysis.

CRediT authorship contribution statement

David Loffreda: Conceptualization, Methodology, Software, Validation, Formal Analysis, Investigation, Resources, Data Curation, Writing-Original Draft, Writing-Review & Editing, Visualization, Project Administration, Funding Acquisition. **Nathalie Tarrat:** Conceptualization, Methodology, Software, Validation, Formal Analysis, Investigation, Resources, Data Curation, Writing-Original Draft, Writing-Review & Editing, Visualization. **Corinne Lacaze- Dufaure:** Writing-Review & Editing. **Franck Rabilloud:** Writing-Review & Editing. **Katia Fajerwerg:** Writing- Review & Editing. **Myrtil L. Kahn:** Writing-Review & Editing. **Vincent Collière:** Investigation, Data Curation. **Christine Lepetit:** Conceptualization, Resources, Data Curation, Writing-Review & Editing. **Pierre Fau:** Conceptualization, Methodology, Validation, Formal Analysis, Investigation, Resources, Data Curation, Writing-Original Draft, Writing- Review & Editing, Visualization.

Declaration of Competing Interest

The authors declare that they have no known competing financial interests or personal relationships that could have appeared to influence the work reported in this paper.

Data availability

The theoretical data supporting the findings of this study can be downloaded from the NOMAD website at the following DOI: 10.17172/NOMAD/2024.05.02–1.

Acknowledgments

These works were developed during the period 2017–2023 in the context of the (DE)CRESCENDO project. The authors thank the PSMN mesocenter in Lyon for the strong support (CPU time and assistance). They also thank GENCI for the access on national HPC resources of IDRIS and TGCC in Paris, and of CINES in Montpellier (project 609). This work was granted access to the HPC resources of CALMIP supercomputing center under the allocations p1303 and p16028.

Appendix A. Supporting information

Supplementary data associated with this article can be found in the online version at doi:10.1016/j.nantod.2025.102662.

References

[1] Y. Xia, X. Xia, Y. Wang, S. Xie, Shape-controlled synthesis of metal nanocrystals, MRS Bull. 38 (2013) 335, https://doi.org/10.1557/mrs.2013.84.
[2] J. Natsuki, T. Natsuki, Y. Hashimoto, A review of silver nanoparticles: synthesis methods, properties and applications, Int. J. Mater. Sci. Appl. 4 (2015) 325, https://doi.org/10.11648/j.ijmsa.20150405.17.
[3] H. You, J. Fang, Particle-mediated nucleation and growth of solution-synthesized metal nanocrystals: a new story beyond the lamer curve, Nano Today 11 (2016) 145–167, https://doi.org/10.1016/j.nantod.2016.04.003.
[4] L.A. Kolahalam, I. KasiViswanath, B.S. Diwakar, B. Govindh, V. Reddy, Y. Murthy, Review on nanomaterials: synthesis and applications, Mater. Today Proc. 18 (2019) 2182–2190, https://doi.org/10.1016/j.matpr.2019.07.371, 2nd International Conference on Applied Sciences and Technology (ICAST-2019): Material Science.
[5] S. Zhou, M. Zhao, T.-H. Yang, Y. Xia, Decahedral nanocrystals of noble metals: synthesis, characterization, and applications, Mater. Today 22 (2019) 108–131, https://doi.org/10.1016/j.mattod.2018.04.003.
[6] C.-J. Jia, F. Schüth, Colloidal metal nanoparticles as a component of designed catalyst, Phys. Chem. Chem. Phys. 13 (2011) 2457–2487, https://doi.org/10.1039/C0CP02680H.
[7] H. Wang, S. Zhou, K.D. Gilroy, Z. Cai, Y. Xia, Icosahedral nanocrystals of noble metals: synthesis and applications, Nano Today 15 (2017) 121–144, https://doi.org/10.1016/j.nantod.2017.06.011.
[8] Q. Zhang, J. Xie, Y. Yu, J.Y. Lee, Monodispersity control in the synthesis of monometallic and bimetallic quasi-spherical gold and silver nanoparticles, Nanoscale 2 (2010) 1962–1975, https://doi.org/10.1039/C0NR00155D.
[9] I. Ghiuta, D. Cristea, 15 - silver nanoparticles for delivery purposes, in: M. Mozafari (Ed.), Nanoengineered Biomaterials for Advanced Drug Delivery, Woodhead Publishing Series in Biomaterials, Elsevier, 2020, pp. 347–371, https://doi.org/10.1016/B978-0-08-102985-5.00015-2.
[10] H. Sharma, P.K. Mishra, S. Talegaonkar, B. Vaidya, Metal nanoparticles: a theranostic nanotool against cancer, Drug Discov. Today 20 (2015) 1143–1151, https://doi.org/10.1016/j.drudis.2015.05.009.
[11] J.R. Morones, J.L. Elechiguerra, A. Camacho, K. Holt, J.B. Kouri, J.T. Ramírez, M. J. Yacaman, The bactericidal effect of silver nanoparticles, Nanotechnology 16 (2005) 2346, https://doi.org/10.1088/0957-4484/16/10/059.
[12] A. Panáček, L. Kvítek, R. Prucek, M. Kolár, R. Večerová, N. Pizúrová, V.K. Sharma, T. Nevěčná, R. Zboril, Silver colloid nanoparticles: synthesis, characterization, and their antibacterial activity, J. Phys. Chem. B 110 (2006) 16248–16253, https://doi.org/10.1021/jp063826h.
[13] B. LeOuay, F. Stellacci, Antibacterial activity of silver nanoparticles: a surface science insight, Nano Today 10 (2015) 339–354, https://doi.org/10.1016/j.nantod.2015.04.002.
[14] D. Reinhard, B.D. Hall, D. Ugarte, R. Monot, Size-independent fcc-to-icosahedral structural transition in unsupported silver clusters: an electron diffraction study of clusters produced by inert-gas aggregation, Phys. Rev. B 55 (1997) 7868–7881, https://doi.org/10.1103/PhysRevB.55.7868.
[15] M.Á. Gracia-Pinilla, D. Ferrer, S. Mejía-Rosales, E. Pérez-Tijerina, Size-selected ag nanoparticles with five-fold symmetry, Nanoscale Res. Lett. 4 (2009) 896, https://doi.org/10.1007/s11671-009-9328-4.
[16] K.D. Gilroy, J. Puibasset, M. Vara, Y. Xia, On the thermodynamics and experimental control of twinning in metal nanocrystals, Angew. Chem. Int. Ed. 56 (2017) 8647–8651, https://doi.org/10.1002/anie.201705443.
[17] I. Barke, H. Hartmann, D. Rupp, L. Flückiger, M. Sauppe, M. Adolph, S. Schorb, C. Bostedt, R. Treusch, C. Peltz, S. Bartling, T. Fennel, K.-H. Meiwes-Broer, T. Möller, The 3d-architecture of individual free silver nanoparticles captured by x-ray scattering, Nat. Commun. 6 (2015) 6187, https://doi.org/10.1038/ncomms7187.
[18] D.M. Foster, Production and characterisation by scanning transmission electron microscopy of size-selected noble metal nanoclusters (Ph.D), University of Birmingham, 2017.
[19] D. Loffreda, D.M. Foster, R.E. Palmer, N. Tarrat, Importance of defective and nonsymmetric structures in silver nanoparticles, J. Phys. Chem. Lett. 12 (2021) 3705–3711, https://doi.org/10.1021/acs.jpclett.1c00259.
[20] J. Vernieres, N. Tarrat, S. Lethbridge, E. Watchorn-Rokutan, T. Slater, D. Loffreda, R.E. Palmer, Influence of air exposure on structural isomers of silver nanoparticles, Commun. Chem. 6 (2023) 19, https://doi.org/10.1038/s42004-023-00813-9.
[21] C. Li, N. Lu, Q. Xu, J. Mei, W. Dong, J. Fu, Z. Cao, Decahedral and icosahedral twin crystals of silver: Formation and morphology evolution, J. Cryst. Growth 319 (2011) 88–95, https://doi.org/10.1016/j.jcrysgro.2011.01.068.
[22] A. Manna, T. Imae, M. Iida, N. Hisamatsu, Formation of silver nanoparticles from a n-hexadecylethylenediamine silver nitrate complex, Langmuir 17 (2001) 6000–6004, https://doi.org/10.1021/la010389j.

[23] Y. Sun, Y. Xia, Shape-controlled synthesis of gold and silver nanoparticles, Science 298 (2002) 2176–2179, https://doi.org/10.1126/science.1077229.
[24] S.D. Bunge, T.J. Boyle, T.J. Headley, Synthesis of coinage-metal nanoparticles from mesityl precursors, Nano Lett. 3 (2003) 901–905, https://doi.org/10.1021/nl034200v.
[25] M. Yamamoto, M. Nakamoto, Novel preparation of monodispersed silver nanoparticles via amine adducts derived from insoluble silver myristate in tertiary alkylamine, J. Mater. Chem. 13 (2003) 2064–2065, https://doi.org/10.1039/B307092A.
[26] S. Nath, S. Praharaj, S. Panigrahi, S. Kundu, S.K. Ghosh, S. Basu, T. Pal, Hexadecylamine capped silver organosol: a substrate for surface enhanced raman scattering, Colloids Surf. A Physicochem. Eng. Asp. 274 (2006) 145–149, https://doi.org/10.1016/j.colsurfa.2005.08.049.
[27] M. Chen, Y.-G. Feng, X. Wang, T.-C. Li, J.-Y. Zhang, D.-J. Qian, Silver nanoparticles capped by oleylamine: formation, growth, and self-organization, Langmuir 23 (2007) 5296–5304, https://doi.org/10.1021/la700553d.
[28] B. Pietrobon, V. Kitaev, Photochemical synthesis of monodisperse size-controlled silver decahedral nanoparticles and their remarkable optical properties, Chem. Mater. 20 (2008) 5186–5190, https://doi.org/10.1021/cm800926u.
[29] D.A. Safin, P.S. Mdluli, N. Revaprasadu, K. Ahmad, M. Afzaal, M. Helliwell, P. O'Brien, E.R. Shakirova, M.G. Babashkina, A. Klein, Nanoparticles and thin films of silver from complexes of derivatives of n-(diisopropylthiophosphoryl)thioureas, Chem. Mater. 21 (2009) 4233–4240, https://doi.org/10.1021/cm901200h.
[30] J. Zeng, Y. Zheng, M. Rycenga, J. Tao, Z.-Y. Li, Q. Zhang, Y. Zhu, Y. Xia, Controlling the shapes of silver nanocrystals with different capping agents, J. Am. Chem. Soc. 132 (2010) 8552–8553, https://doi.org/10.1021/ja103655f.
[31] Q. Zhang, J. Xie, J. Yang, J.Y. Lee, Monodisperse icosahedral ag, au, and pd nanoparticles: size control strategy and superlattice formation, ACS Nano 3 (2009) 139–148, https://doi.org/10.1021/nn800531q.
[32] S. Peng, J.M. McMahon, G.C. Schatz, S.K. Gray, Y. Sun, Reversing the size-dependence of surface plasmon resonances, Proc. Natl. Acad. Sci. 107 (2010) 14530–14534, https://doi.org/10.1073/pnas.1007524107.
[33] M. Tsuji, M. Ogino, R. Matsuo, H. Kumagae, S. Hikino, T. Kim, S.-H. Yoon, Stepwise growth of decahedral and icosahedral silver nanocrystals in dmf, Cryst. Growth Des. 10 (2010) 296–301, https://doi.org/10.1021/cg9009042.
[34] L. Kuai, B. Geng, S. Wang, Y. Zhao, Y. Luo, H. Jiang, Silver and gold icosahedra: one-pot water-based synthesis and their superior performance in the electrocatalysis for oxygen reduction reactions in alkaline media, Chem. A Eur. J. 17 (2011) 3482–3489, https://doi.org/10.1002/chem.201002949.
[35] X. Hou, X. Zhang, Y. Fang, S. Chen, N. Li, Q. Zhou, 1-hexadecylamine as both reducing agent and stabilizer to synthesize au and ag nanoparticles and their sers application, J. Nanopart. Res. 13 (2011) 1929, https://doi.org/10.1007/s11051-010-9945-y.
[36] Y. Wang, D. Wan, S. Xie, X. Xia, C.Z. Huang, Y. Xia, Synthesis of silver octahedra with controlled sizes and optical properties via seed-mediated growth, ACS Nano 7 (2013) 4586–4594, https://doi.org/10.1021/nn401363e.
[37] R. Keunen, N. Cathcart, V. Kitaev, Plasmon mediated shape and size selective synthesis of icosahedral silver nanoparticles via oxidative etching and their 1-d transformation to pentagonal pins, Nanoscale 6 (2014) 8045–8051, https://doi.org/10.1039/C4NR01477D.
[38] J. Cure, Y. Coppel, T. Dammak, P.F. Fazzini, A. Mlayah, B. Chaudret, P. Fau, Monitoring the coordination of amine ligands on silver nanoparticles using nmr and sers, Langmuir 31 (2015) 1362–1367, https://doi.org/10.1021/la504715f.
[39] Z.-X. Xie, W.-C. Tzeng, C.-L. Huang, One-pot synthesis of icosahedral silver nanoparticles by using a photoassisted tartrate reduction method under uv light with a wavelength of 310 nm, ChemPhysChem 17 (2016) 2551–2557, https://doi.org/10.1002/cphc.201600257.
[40] H. Yang, Y. Wang, X. Chen, X. Zhao, L. Gu, H. Huang, J. Yan, C. Xu, G. Li, J. Wu, A. J. Edwards, B. Dittrich, Z. Tang, D. Wang, L. Lehtovaara, H. Häkkinen, N. Zheng, Plasmonic twinned silver nanoparticles with molecular precision, Nat. Commun. 7 (2016) 12809, https://doi.org/10.1038/ncomms12809.
[41] W. Wang, S. Zhou, M. Shen, Z.D. Hood, K. Xiao, Y. Xia, Facile synthesis of silver icosahedral nanocrystals with uniform and controllable sizes, ChemNanoMat 4 (2018) 1071, https://doi.org/10.1002/cnma.201800255.
[42] S.-F. Yuan, Z.-J. Guan, W.-D. Liu, Q.-M. Wang, Solvent-triggered reversible interconversion of all-nitrogen-donor-protected silver nanoclusters and their responsive optical properties, Nat. Commun. 10 (2019) 4032, https://doi.org/10.1038/s41467-019-11988-y.
[43] J.-Y. Liu, F. Alkan, Z. Wang, Z.-Y. Zhang, M. Kurmoo, Z. Yan, Q.-Q. Zhao, C. M. Aikens, C.-H. Tung, D. Sun, Different silver nanoparticles in one crystal: Ag210 (iprphs)71(ph3p)5cl and ag211(iprphs)71(ph3p)6cl, Angew. Chem. Int. Ed. 58 (2019) 195–199, https://doi.org/10.1002/anie.201810772.
[44] S.K. Gautam, Y. Baid, P.T. Magar, T.R. Binadi, B. Regmi, Antimicrobial study of green synthesized silver nanoparticles (agnps) by using Ageratina adenophora and its characterization, Int. J. Appl. Sci. Biotechnol. 9 (2021) 128–132, https://doi.org/10.3126/ijasbt.v9i2.37822.
[45] F. Hu, H.-W. Luyang, R.-L. He, Z.-J. Guan, S.-F. Yuan, Q.-M. Wang, Face-centered cubic silver nanoclusters consolidated with tetradentate formamidinate ligands, J. Am. Chem. Soc. 144 (2022) 19365–19371, https://doi.org/10.1021/jacs.2c07018.
[46] K.A. Fichthorn, Theory of anisotropic metal nanostructures, Chem. Rev. 123 (2023) 4146–4183, https://doi.org/10.1021/acs.chemrev.2c00831.
[47] T. Yan, H. Zhang, K.A. Fichthorn, Minimum free-energy shapes of ag nanocrystals: vacuum vs solution, ACS Nano 17 (2023) 19288–19304, https://doi.org/10.1021/acsnano.3c06395.
[48] C. Mottet, G. Tréglia, B. Legrand, New magic numbers in metallic clusters: an unexpected metal dependence, Surf. Sci. 383 (1997) L719–L727, https://doi.org/10.1016/S0039-6028(97)00226-4.
[49] F. Baletto, C. Mottet, R. Ferrando, Microscopic mechanisms of the growth of metastable silver icosahedra, Phys. Rev. B 63 (2001) 155408, https://doi.org/10.1103/PhysRevB.63.155408.
[50] J.P.K. Doye, F. Calvo, Entropic effects on the size dependence of cluster structure, Phys. Rev. Lett. 86 (2001) 3570–3573, https://doi.org/10.1103/PhysRevLett.86.3570.
[51] F. Baletto, R. Ferrando, A. Fortunelli, F. Montalenti, C. Mottet, Crossover among structural motifs in transition and noble-metal clusters, J. Chem. Phys. 116 (2002) 3856–3863, https://doi.org/10.1063/1.1448484.
[52] G.A. Narvaez, J. Kim, J.W. Wilkins, Effects of morphology on phonons in nanoscopic silver grains, Phys. Rev. B 72 (2005) 155411, https://doi.org/10.1103/PhysRevB.72.155411.
[53] X. Shao, X. Yang, W. Cai, Geometry optimization and structural distribution of silver clusters from ag170 to ag310, Chem. Phys. Lett. 460 (2008) 315–318, https://doi.org/10.1016/j.cplett.2008.05.031.
[54] C. Amano, H. Niina, Y. Mikami, Molecular dynamics on silver cluster structures along the icosahedral noncrystalline and the cuboctahedral c.c.p. growth sequence, J. Mol. Struct. Theochem 904 (2009) 64–68, https://doi.org/10.1016/j.theochem.2009.02.030.
[55] B. Wang, M. Liu, Y. Wang, X. Chen, Structures and energetics of silver and gold nanoparticles, J. Phys. Chem. C. 115 (2011) 11374–11381, https://doi.org/10.1021/jp201023x.
[56] A.L. González, C. Noguez, J. Beránek, A.S. Barnard, Size, shape, stability, and color of plasmonic silver nanoparticles, J. Phys. Chem. C. 118 (2014) 9128–9136, https://doi.org/10.1021/jp5018168.
[57] J.M. Rahm, P. Erhart, Beyond magic numbers: atomic scale equilibrium nanoparticle shapes for any size, Nano Lett. 17 (2017) 5775–5781, https://doi.org/10.1021/acs.nanolett.7b02761.
[58] M.M. Blazhynska, A. Kyrychenko, O.N. Kalugin, Molecular dynamics simulation of the size-dependent morphological stability of cubic shape silver nanoparticles, Mol. Simul. 44 (2018) 981–991, https://doi.org/10.1080/08927022.2018.1469751.
[59] M. Settem, C. Roncaglia, R. Ferrando, A. Giacomello, Structural transformations in Cu, Ag, and Au metal nanoclusters, J. Chem. Phys. 159 (2023) 094303, https://doi.org/10.1063/5.0159257.
[60] E. Panizon, D. Bochicchio, G. Rossi, R. Ferrando, Tuning the structure of nanoparticles by small concentrations of impurities, Chem. Mater. 26 (2014) 3354–3356, https://doi.org/10.1021/cm501001f.
[61] H. Sultana, E. Lee, Elucidating the formation mechanisms of silver nanoparticles from a comprehensive simulation based on first-principles calculations, J. Phys. Chem. C. 122 (2018) 1333–1344, https://doi.org/10.1021/acs.jpcc.7b09991.
[62] M. Tobita, Y. Yasuda, Theoretical and experimental vibrational characterizations of amine-coated silver nanoparticles, J. Phys. Chem. C. 112 (2008) 13851–13855, https://doi.org/10.1021/jp803195e.
[63] L.-B. Zhao, R. Huang, M.-X. Bai, D.-Y. Wu, Z.-Q. Tian, Effect of aromatic amine-metal interaction on surface vibrational raman spectroscopy of adsorbed molecules investigated by density functional theory, J. Phys. Chem. C. 115 (2011) 4174–4183, https://doi.org/10.1021/jp1117135.
[64] P.V. Nhat, N.T. Si, N.T. Tien, M.T. Nguyen, Theoretical study of the binding of the thiol-containing cysteine amino acid to the silver surface using a cluster model, J. Phys. Chem. A 125 (2021) 3244–3256, https://doi.org/10.1021/acs.jpca.0c11182.
[65] C. Lacaze-Dufaure, Y. Bulteau, N. Tarrat, D. Loffreda, P. Fau, K. Fajerwerg, M. L. Kahn, F. Rabilloud, C. Lepetit, Coordination of ethylamine on small silver clusters: structural and topological (elf, qtaim) analyses, Inorg. Chem. 61 (2022) 7274–7285, https://doi.org/10.1021/acs.inorgchem.1c03870.
[66] N. Tarrat, D. Loffreda, Morphological sensitivity of silver nanoparticles to the environment, Environ. Sci. Nano 10 (2023) 1754, https://doi.org/10.1039/D2EN01129H.
[67] H. Sellers, A. Ulman, Y. Shnidman, J.E. Eilers, Structure and binding of alkanethiolates on gold and silver surfaces: implications for self-assembled monolayers, J. Am. Chem. Soc. 115 (1993) 9389–9401, https://doi.org/10.1021/ja00074a004.
[68] J.Q. Hou, H.S. Kang, K.W. Kim, J.R. Hahn, Binding characteristics of pyridine on Ag(110), J. Chem. Phys. 128 (2008) 134707, https://doi.org/10.1063/1.2888932.
[69] J.R. Hahn, H.S. Kang, Role of molecular orientation in vibration, hopping, and electronic properties of single pyridine molecules adsorbed on ag(110) surface: a combined stm and dft study, Surf. Sci. 604 (2010) 258–264, https://doi.org/10.1016/j.susc.2009.11.014.
[70] G. Mercurio, E.R. McNellis, I. Martin, S. Hagen, F. Leyssner, S. Soubatch, J. Meyer, M. Wolf, P. Tegeder, F.S. Tautz, K. Reuter, Structure and energetics of azobenzene on ag(111): benchmarking semiempirical dispersion correction approaches, Phys. Rev. Lett. 104 (2010) 036102, https://doi.org/10.1103/PhysRevLett.104.036102.
[71] T. Chen, A. Pal, J. Gao, Y. Han, H. Chen, S. Sukhishvili, H. Du, S.G. Podkolzin, Identification of vertical and horizontal configurations for bpe adsorption on silver surfaces, J. Phys. Chem. C. 119 (2015) 24475–24488, https://doi.org/10.1021/acs.jpcc.5b07831.
[72] A.C. Ngandjong, C. Mottet, J. Puibasset, Influence of the silica support on the structure and the morphology of silver nanoparticles: a molecular simulation study, J. Phys. Chem. C. 120 (2016) 8323–8332, https://doi.org/10.1021/acs.jpcc.6b00290.
[73] A.C. Ngandjong, C. Mottet, J. Puibasset, Freezing and melting of silver nanoparticles on silica substrate using a simple interatomic potential for ag-sio2

interaction on the basis of ab initio calculations and experimental data, J. Phys. Chem. C. 121 (2017) 3615–3622, https://doi.org/10.1021/acs.jpcc.6b12084.
[74] A. Lahouari, J.-P. Piquemal, J. Richardi, Reaxff simulations of self-assembled monolayers on silver surfaces and nanocrystals, J. Phys. Chem. C. 128 (2024) 1193–1201, https://doi.org/10.1021/acs.jpcc.3c07098.
[75] K. Rossi, Multiscale modelling of metallic nanoparticles structural and catalytic properties, King's College London Ph.D. (2019).
[76] M. Huš, M. Grilc, A. Pavlišič, B. Likozar, A. Hellman, Multiscale modelling from quantum level to reactor scale: an example of ethylene epoxidation on silver catalysts, Catal. Today 338 (2019) 128–140, https://doi.org/10.1016/j.cattod.2019.05.022.
[77] J. Subbotina, V. Lobaskin, Multiscale modeling of bio-nano interactions of zero-valent silver nanoparticles, J. Phys. Chem. B 126 (2022) 1301–1314, https://doi.org/10.1021/acs.jpcb.1c09525.
[78] K.A. Fichthorn, Atomic-scale theory and simulations for colloidal metal nanocrystal growth, J. Chem. Eng. Data 59 (2014) 3113–3119, https://doi.org/10.1021/je500189s.
[79] C. Zeni, K. Rossi, A. Glielmo, A. Fekete, N. Gaston, F. Baletto, A.De Vita, Building machine learning force fields for nanoclusters, J. Chem. Phys. 148 (2018) 241739, https://doi.org/10.1063/1.5024558.
[80] B. Wiley, T. Herricks, Y. Sun, Y. Xia, Polyol synthesis of silver nanoparticles: use of chloride and oxygen to promote the formation of single-crystal, truncated cubes and tetrahedrons, Nano Lett. 4 (2004) 1733–1739, https://doi.org/10.1021/nl048912c.
[81] A. Andrieux-Ledier, B. Tremblay, A. Courty, Synthesis of silver nanoparticles using different silver phosphine precursors: formation mechanism and size control, J. Phys. Chem. C. 117 (2013) 14850–14857, https://doi.org/10.1021/jp4040248.
[82] B.S. Lim, A. Rahtu, J.-S. Park, R.G. Gordon, Synthesis and characterization of volatile, thermally stable, reactive transition metal amidinates, Inorg. Chem. 42 (2003) 7951–7958, https://doi.org/10.1021/ic0345424.
[83] M. Puyo, P. Fau, M.L. Kahn, D. Mesguich, J. Launay, K. Fajerwerg, Removable composite electrode made of silver nanoparticles on pyrolyzed photoresist film for the electroreduction of 4-nitrophenol, Langmuir 35 (2019) 14194–14202, https://doi.org/10.1021/acs.langmuir.9b02405.
[84] K. Koga, K. Sugawara, Population statistics of gold nanoparticle morphologies: direct determination by hrem observations, Surf. Sci. 529 (2003) 23–35, https://doi.org/10.1016/S0039-6028(03)00300-5.
[85] W. Qi, Nanoscopic thermodynamics, Acc. Chem. Res. 49 (2016) 1587–1595, https://doi.org/10.1021/acs.accounts.6b00205.
[86] P.J. Edwards, S. Stuart, J.T. Farmer, R. Shi, R. Long, O.V. Prezhdo, V.V. Kresin, Substrate-selective adhesion of metal nanoparticles to graphene devices, J. Phys. Chem. Lett. 14 (2023) 6414–6421, https://doi.org/10.1021/acs.jpclett.3c01542.
[87] G. Kresse, J. Hafner, Ab initio molecular dynamics for liquid metals, Phys. Rev. B 47 (1993) 558–561, https://doi.org/10.1103/PhysRevB.47.558.
[88] G. Kresse, J. Furthmüller, Efficiency of ab-initio total energy calculations for metals and semiconductors using a plane-wave basis set, Comput. Mater. Sci. 6 (1996) 15–50, https://doi.org/10.1016/0927-0256(96)00008-0.
[89] G. Kresse, J. Furthmüller, Efficient iterative schemes for ab initio total-energy calculations using a plane-wave basis set, Phys. Rev. B 54 (1996) 11169–11186, https://doi.org/10.1103/PhysRevB.54.11169.
[90] S. Grimme, J. Antony, S. Ehrlich, H. Krieg, A consistent and accurate ab initio parametrization of density functional dispersion correction (dft-d) for the 94 elements h-pu, J. Chem. Phys. 132 (2010) 154104, https://doi.org/10.1063/1.3382344.
[91] G. Kresse, D. Joubert, From ultrasoft pseudopotentials to the projector augmented-wave method, Phys. Rev. B 59 (1999) 1758–1775, https://doi.org/10.1103/PhysRevB.59.1758.
[92] K. Mathew, V.S.C. Kolluru, R.G. Hennig, Vaspsol: Implicit solvation and electrolyte model for density-functional theory, ⟨https://github.com/henniggroup/VASPsol⟩, 2018.10.5281/zenodo.2555053.
[93] K. Mathew, R. Sundararaman, K. Letchworth-Weaver, T.A. Arias, R.G. Hennig, Implicit solvation model for density-functional study of nanocrystal surfaces and reaction pathways, J. Chem. Phys. 140 (2014) 084106, https://doi.org/10.1063/1.4865107.
[94] K. Mathew, V.S.C. Kolluru, S. Mula, S.N. Steinmann, R.G. Hennig, Implicit self-consistent electrolyte model in plane-wave density-functional theory, J. Chem. Phys. 151 (2019) 234101, https://doi.org/10.1063/1.5132354.

David Loffreda is a CNRS research director, working in the Laboratory of Chemistry of Ecole Normale Supérieure de Lyon and chairing the scientific committee of theoretical chemistry at GENCI (Paris). He began his career at the Institut de Recherches sur la Catalyse et l'Environnement de Lyon. He is an expert in the description of the electronic structure of chemical systems and complex reactive interfaces, by using periodic density functional theory. He developed a code called Phonon allowing the theoretical prediction of metallic, molecular vibrations and infrared spectra in heterogeneous catalysis. Over the years, he has been developing DFT models of metallic nanoparticles for various applications in chemistry, physics, catalysis and radiotherapy.

Nathalie Tarrat is Researcher at CNRS, Centre for Materials Elaboration and Structural Studies (CEMES), Toulouse, France. She obtained a PhD in theoretical physical chemistry and chemistry-biology from Toulouse University (2005), for her work on phosphate esters hydrolysis. After 5 years of post-doctoral training dedicated to the study of solvent effects and condensed matter, she joined the CNRS in 2010 in the Toulouse Biotechnology Institute (TBI) laboratory to work on rational design of enzymes. Since 2013, she develops at CEMES an activity focused on bio-functional nanoparticles in their various life-cycle stages and associated environments, mainly to design safer-by-design nano-antimicrobials.

Corinne Lacaze-Dufaure is a professor at University of Toulouse (France) and she is developing research activities at the Interuniversity Center for Materials Research and Engineering (CIRIMAT). She is particularly interested in electronic-structure calculations of materials surfaces (DFT) and phenomena thereon, relevant, on the one hand, to the protection of metals against corrosion and, on the other hand, to the functionalisation of materials of biomedical interest.

Franck Rabilloud Franck Rabilloud received his PhD degree in 2000 from University Toulouse 3, France. After a postdoctoral position at the University of Valladolid, Spain, he got an academic position at University Lyon 1 in 2001. He is head of the team "Theoretical Physical Chemistry" at Institute for Light and Matter. His research mainly focuses on method development in electronic structure theory with an emphasis on light - nanoparticles interaction and electron - molecules collisions.

Myrtil L. Kahn is currently Director of Research at the CNRS Coordination Chemistry Laboratory in Toulouse, where she heads the "Nanochemistry, organization and sensors" team. Her main research interests concern nanosciences and their applications in relation to major societal challenges such as aeronautics, energy, the environment, microelectronics and health. Her research focuses on the design and development of complex nano-objects and hybrid nanomaterials, from precursor synthesis to devices. She is co-author of over 120 articles and 11 patents.

Pierre Fau obtained his Ph.D. in Materials Science from the Université Paul Sabatier in 1993. He worked for 10 years in the microelectronic industry for the development of nanostructured MOS gas sensors as research engineer in Motorola Toulouse and then as R&D Director in MiCS (Neuchatel, Switzerland). In 2005 he held a position of research engineer at LCC-CNRS up to 2022 where he moved to LPCNO-INSA in the "Nanostructures et Chimie Organométallique" team. His research activity deals with synthesis and characterization of nanostructured materials (metal and metal oxides, in solution or on substrates, powders, CNTs …) for gas sensors, electronics, catalysis (magnetic induction, photocatalysis) applications. He holds 65 peer-reviewed publications.